



OPEN Hybrid attention structure preserving network for reconstruction of under-sampled OCT images

Ze Zhao Guo & Zhanfang Zhao

Optical coherence tomography (OCT) is a non-invasive, high-resolution imaging technology that provides cross-sectional images of tissues. Dense acquisition of A-scans along the fast axis is required to obtain high digital resolution images. However, the dense acquisition will increase the acquisition time, causing the discomfort of patients. In addition, the longer acquisition time may lead to motion artifacts, thereby reducing imaging quality. In this work, we proposed a hybrid attention structure preserving network (HASP) to achieve super-resolution of under-sampled OCT images to speed up the acquisition. It utilized adaptive dilated convolution-based channel attention (ADCCA) and enhanced spatial attention (ESA) to better capture the channel and spatial information of the feature. Moreover, convolutional neural networks (CNNs) exhibit a higher sensitivity of low-frequency than high-frequency information, which may lead to a limited performance on reconstructing fine structures. To address this problem, we introduced an additional branch, i.e., textures & details branch, using high-frequency decomposition images to better super-resolve retinal structures. The superiority of our method was demonstrated by qualitative and quantitative comparisons with mainstream methods. Furthermore, HASP was applied to three out-of-distribution datasets, validating its strong generalization capability.

Keywords Optical coherence tomography, Super-resolution, Attention mechanism

Optical coherence tomography (OCT) is a non-invasive optical imaging technique¹. Due to its cellular-level imaging resolution, it has been widely used in ophthalmology, dermatology, and cardiology^{2–4}. OCT's high-resolution imaging capability allows for detailed visualization of retinal structures, enabling early detection and monitoring of various retinal conditions, such as age-related macular degeneration (AMD)⁵, diabetic retinopathy⁶, and glaucoma⁷. The ability to capture cross-sectional images of the retina in vivo has revolutionized the field of ophthalmology, providing clinicians with critical information that influences diagnosis and treatment plans.

Typically, dense acquisition is required to capture fine microstructures of the sample. However, conducting dense acquisition, especially over a large field of view, will decrease the imaging speed and thereby cause the discomfort of patients. Moreover, the longer acquisition time is likely to exacerbate eye motion, introducing artifacts into the image⁸. Down-sampling is the easiest way to speed up the acquisition, however, at the sacrifice of the resolution.

To improve the digital resolution of under-sampled images, various conventional methods have been proposed. Fang et al. proposed a sparsity-based framework that simultaneously performed interpolation and denoising to reconstruct OCT images efficiently⁹. Abbasi et al. introduced a non-local weighted sparse representation (NWSR) method, which integrates sparse representations of multiple noisy and denoised patches to improve image quality¹⁰. Wang et al. proposed to utilize compressive sensing (CS) and digital filters to enhance the down-sampled OCT angiography images¹¹. The study demonstrated that the vascular structures could be well reconstructed through CS with a sampling rate on B-scans at 70%, suggesting that CS could significantly accelerate acquisition in the OCT system. However, the traditional methods tend to perform poorly at high scale factors. Specifically, these methods have difficulty in reconstructing OCT images with high accuracy and may lead to artifacts at high scale factors. Hence, they cannot be applied in some scenarios where low scan density is required.

College of Information and Engineering, Hebei GEO University, Hebei, China. email: zhaozhanfang@hgu.edu.cn

In recent years, deep learning methods have been popular among various medical image processing tasks^{12–14}. Huang et al. utilized a generative adversarial network (GAN) to super-resolve OCT images while reducing the noise, introducing deep learning into OCT super-resolution for the first time¹⁵. Qiu et al. proposed a novel semi-supervised method using UNet and DBPN to achieve simultaneous super-resolution and denoising¹⁶. However, these deep-learning-based super-resolution networks ignore the fact that convolutional neural network (CNN) is more sensitive to low-frequency information¹⁷, potentially limiting the performance on reconstructing fine-grained structures in OCT images. With the success of transformers in the field of computer vision¹⁸, many researchers have successfully applied transformers to OCT super-resolution¹⁹. Yao et al. proposed the PSCAT²⁰ composed of window self-attention²¹ and CBAM²² to achieve denoising and super-resolution simultaneously. Lu et al. presented a pyramid long-range transformer TESR²³ to reconstruct under-sampled OCT images. Furthermore, the transformer was integrated with the CNN to leverage their complementary strengths, i.e., global dependency and local dependency, for OCT super-resolution²⁴.

To obtain high digital resolution images within a short acquisition time, we proposed a novel OCT super-resolution model named hybrid attention structure preserving network (HASPEN). HASPEN has two branches. One branch was used to primarily restore the low-frequency features of images. The another branch could enhance the perceptual quality of the output by learning the high-frequency features of decomposed images. The low-frequency and high-frequency features from the two branches were concatenated over channels to fuse the information. Additionally, the hybrid attention mechanism was introduced to enhance the network's capacity to learn spatial and channel information, improving the reconstruction capability. Next, we utilized the public retinal OCT image dataset OCT2017 to test HASPEN at different sampling rates. Compared with the current mainstream methods, HASPEN achieved the best results at 4x and 8x SR. Moreover, we investigated the impact of network depths and widths on performance and conducted ablation studies to validate the effectiveness of our key components and hybrid loss. Finally, the experiment demonstrated that our proposed HASPEN exhibited strong generalization capabilities for diabetic macular edema (DME), choroidal neovascularization (CNV), and drusen in early AMD which was unseen during training.

Methods

Data preparation

In this paper, we utilized the retinal OCT image dataset OCT2017²⁵. The original dataset contains 84,495 images in total, covering normal and abnormal retinal images. From the subset of normal retinal images, 1,300 images were selected for the training set, 200 images for the validation set, and 100 images for the testing set.

Considering the limited GPU resources, the images were randomly cropped into 256×256 as the high-resolution (HR) ground truth. To generate low-resolution (LR) images, we under-sampled the columns of the ground truth, obtaining 2x, 4x, and 8x images. Subsequently, the LR-HR image pairs were obtained. In addition, 100 OCT images of DME, CNV, and DRUSEN from the OCT2017 dataset were utilized to create corresponding sub-datasets for validating the network's generalization capability.

Image decomposition

Unsharp masking (USM) is commonly employed in image processing to enhance high-frequency details²⁶. To be specific, The original image is subtracted by its blurred version to generate a residual image. This residual image is then added back to the original image to enhance edges and details. Its specific steps are as follows:

$$R = O - B, \quad (1)$$

$$S = O + k(R), \quad (2)$$

where O , B , R represent the original image, the blurred image, and the residual image (high-frequency image). k is the scaling coefficient used to adjust the degree of sharpening, while S is the sharpened image.

Xu et al. demonstrated that CNN exhibited a greater sensitivity to low-frequency information than high-frequency information¹⁷. However, high-frequency information is essential for reconstructing fine details. To address this problem, we proposed an approach inspired by USM that involved decomposing images into a residual image enriched with high-frequency content. This residual image was subsequently input into an additional branch to enhance the reconstruction of high-frequency features. Specifically, a Gaussian filter with a kernel size of 5×5 and a kernel standard deviation of 1.5 in the X direction was applied to blur the image. Then, the high-frequency image could be obtained by subtraction. Both LR and HR images were decomposed to generate the corresponding high-frequency images. Different from the Eq. 2, we utilized a textures & details CNN branch to enhance edges and details. The outputs of the original branch and the textures & details branch will then be concatenated and fused to generate the final image.

Hybrid attention mechanism

Previous studies have proven the effectiveness of attention mechanisms in super-resolution tasks²⁷. It can enable the network to focus on important features, thereby enhancing the quality of reconstruction. As shown in Fig. 1, we designed a hybrid attention mechanism, i.e., intra-block and inter-block attention. First, we integrated an enhanced spatial attention (ESA)²⁸ in the spatial attention residual block (SARB). Initially, a 1×1 convolutional layer was performed to reduce the channel dimension, thereby decreasing the computational complexity of the ESA module. And then, a 3×3 convolutional layer with a stride of 2 was utilized to reduce the resolution of the feature map by half. Next, a 7×7 max pooling with a stride of 3 was used to achieve downsampling and enlarge the receptive field. Subsequently, a 3×3 convolutional layer was used for feature extraction. Bilinear interpolation and 1×1 Conv were utilized to recover the spatial and channel dimensions, respectively. Finally,

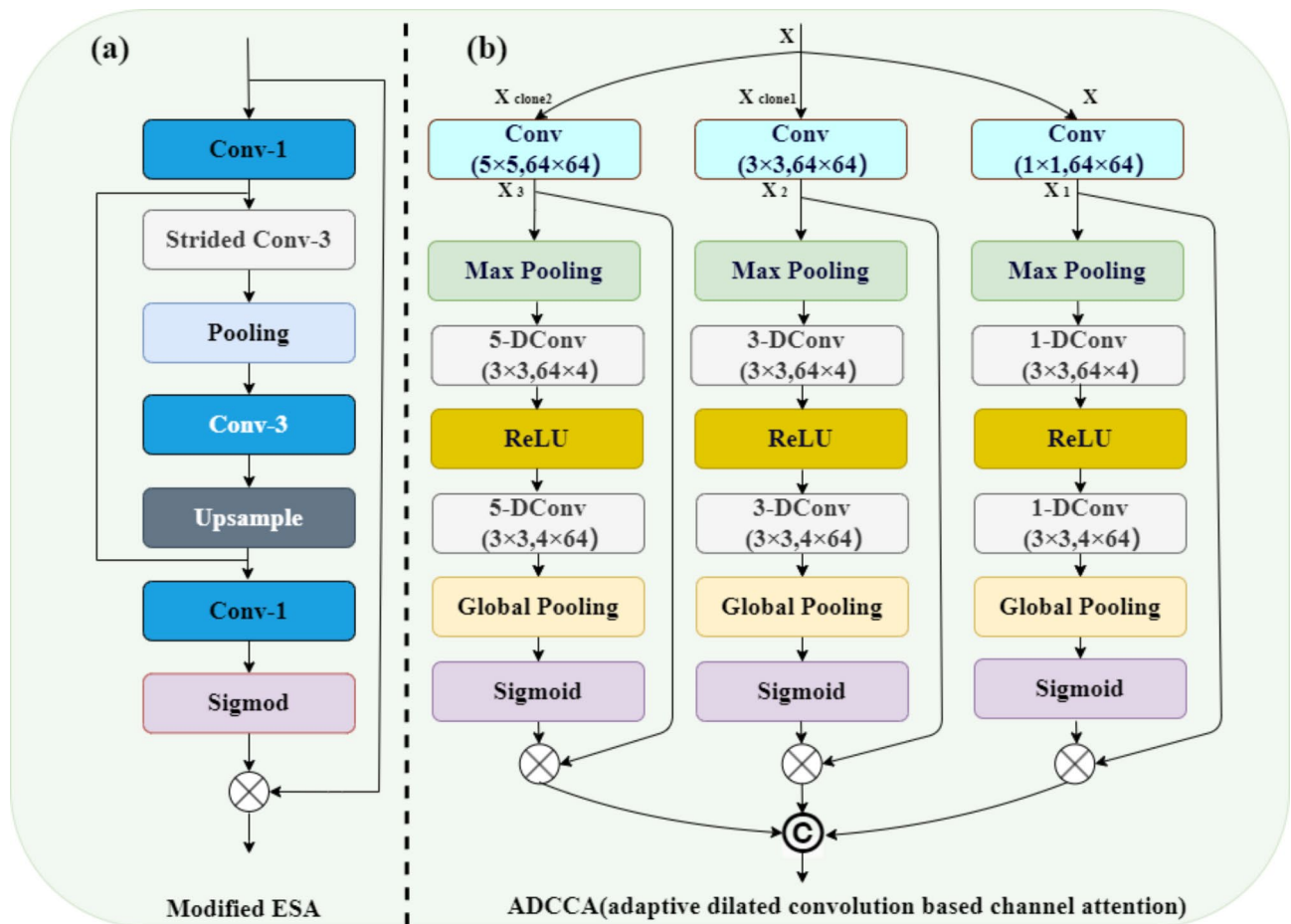


Fig. 1. Hybrid attention mechanism in HASPN. (a) Modified ESA, where Conv-N represents a $N \times N$ convolutional layer. (b) ADCCA, where N-DConv ($k \times k, i \times o$) denotes a $k \times k$ convolutional layer with a dilation factor of N, input channel of i, and output channel of o.

the input of ESA was dotted with the attention score matrix. Different from the conventional ESA, we did not use Conv Group (two Conv(3×3)-ReLU and one Conv(3×3)) to extract features. We experimentally found that using a 3×3 convolution for feature extraction was better than using the Conv Group in the original ESA. Specifically, utilizing 3×3 Conv for feature extraction yielded a notable enhancement in PSNR, demonstrating an increase of 1.87dB, as well as an improvement in SSIM, which exhibited a rise of 0.017, in comparison to the use of Conv Group. That means adopting a single 3×3 convolutional layer not only significantly reduces the model's computational complexity but also achieves better performance. As shown in Fig. 2, the output feature map of ESA displays more distinct retinal layers compared to the original one. It demonstrates that ESA enables the network to focus on specific spatial regions, leading to a better performance.

Secondly, to further enhance the ability of the network to distinguish the importance of different channels, adaptive dilated convolution-based channel attention (ADCCA) was incorporated every M SARBs (as shown in Fig. 3). ADCCA exploits kernels of different sizes and different dilated factors (1, 3, 5) to enrich the receptive field of convolution, thereby capturing information of various scales. Similar to SENet²⁹, ADCCA first performs a squeeze operation using max pooling to reduce the resolution of the feature maps by half. Then, it follows with an excitation step, which involves dilated Conv-ReLU-dilated Conv (DC-ReLU-DC) operations with different dilated factors. Subsequently, a global pooling is used to decrease the resolution of feature maps to 1×1 to obtain the attention of each channel.

Super resolution network framework

Inspired by the TDPN³⁰, we proposed a novel network named HASPN as shown in Fig. 3. The network contained two parallel branches: one branch was responsible for restoring the coarse image, while the other branch focused on the restoration of fine textures and details. In addition, we implemented a dual-branch weight-sharing strategy. This approach not only increases the connection between dual branches but also significantly reduces the number of parameters. The outputs of the two branches were finally integrated through a fusion module to generate super-resolution images.

Each branch consisted of three parts: shallow feature extraction, deep feature extraction, and upsampling reconstruction. In the shallow feature extraction stage, a 3×3 convolutional layer was used to extract the shallow

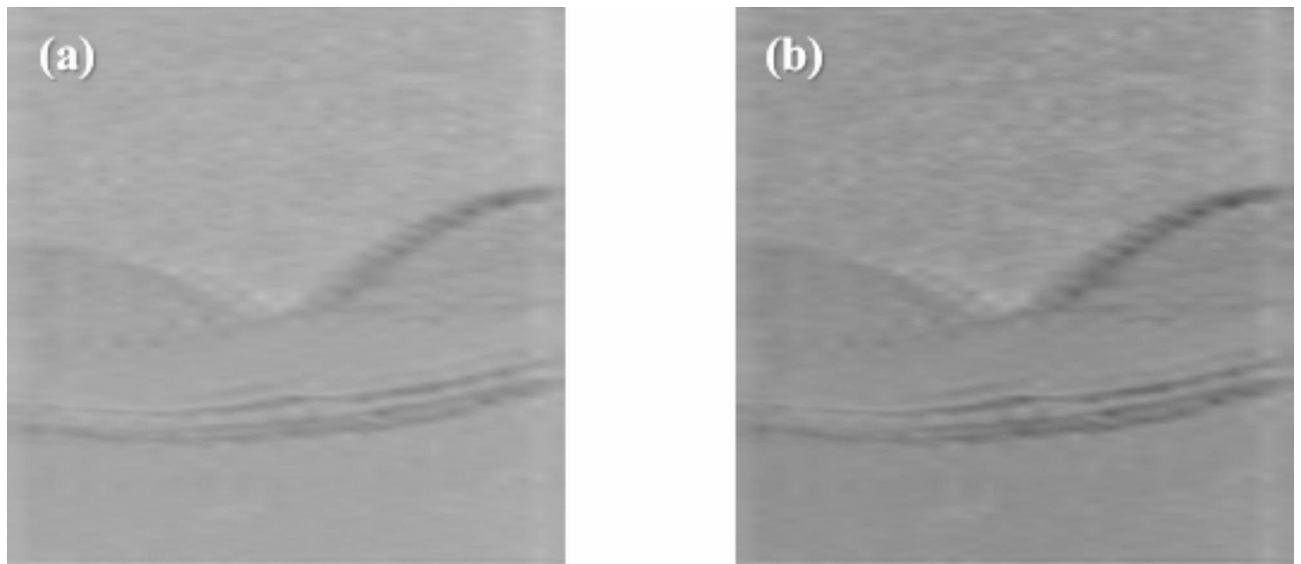


Fig. 2. Visualization of feature maps. (a) The input feature map of ESA. (b) The output feature map of ESA.

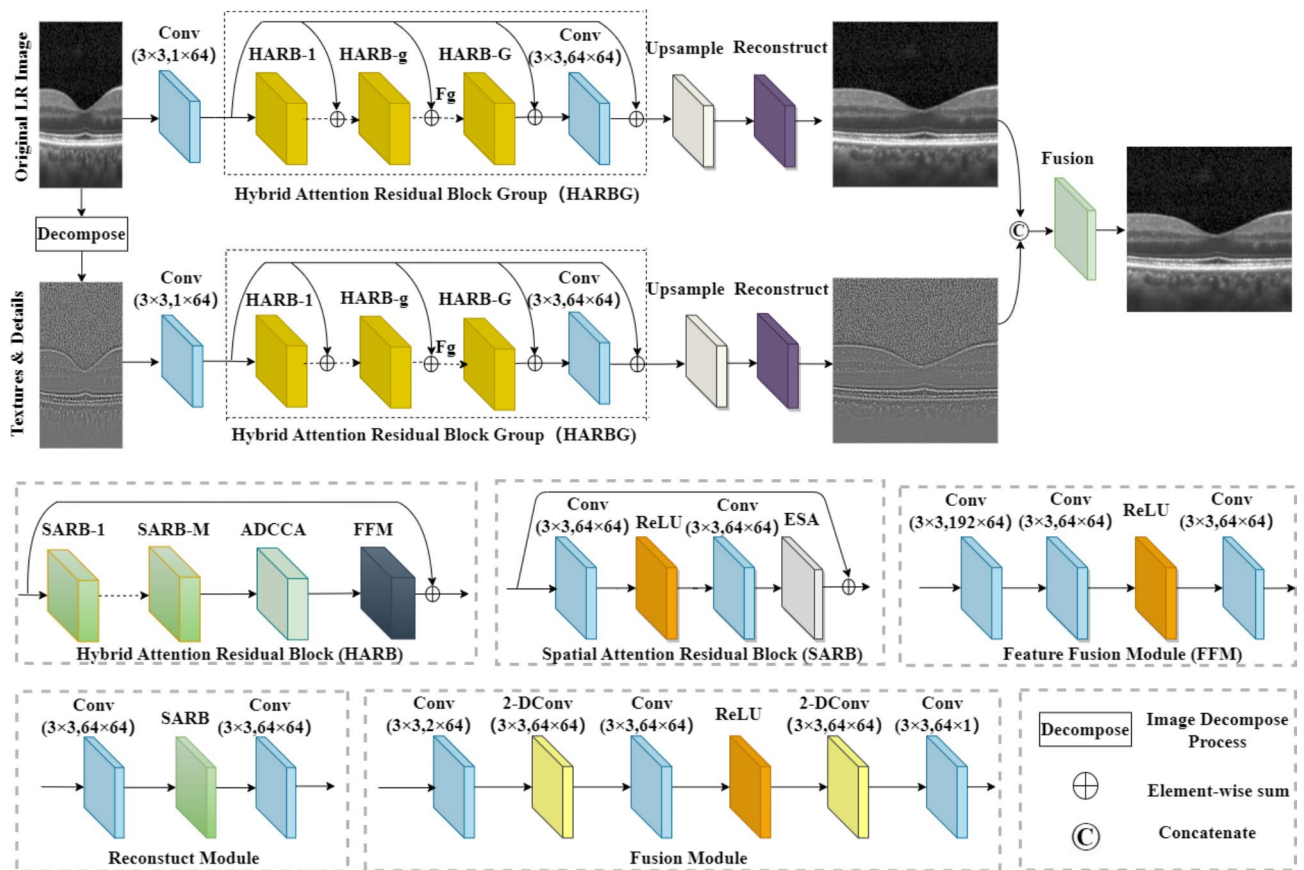


Fig. 3. Framework of the proposed HASPN.

features of the network. These features were then fed to each hybrid attention residual block group (HARBG) module through the skip connections from the shared source to help the network better focus on high-frequency features. Deep feature extraction consisted of multiple hybrid attention residual block (HARB) units and a 3×3 convolutional layer. Each HARB unit consisted of M SARBs, an ADCCA, and a feature fusion module (FFM). ESA was introduced into SARB to allow the network focus on some important spatial features, significantly

enhancing the perceptual quality of reconstructed images in super-resolution. After processed by multiple SARB units, multi-scale information was extracted by ADCCA which adaptively used convolutions of various sizes and different dilation factors. In addition, it made the network focus more on key feature channels effectively. Finally, FFM was used to merge feature maps at various scales in ADCCA.

Bilinear interpolation was utilized as the horizontal upsampling method. The reconstruction module contained a 3×3 Conv, a SARB, and another 3×3 Conv. Finally, the coarse image reconstructed by the original LR image branch and the high-frequency image reconstructed by the textures & details branch were concatenated over channel and fused together. The fusion module has a similar structure to the FFM, with one key difference: it incorporates a 2-DConv between every two convolutional layers. This modification enables the fusion module to capture a larger receptive field and integrate a wider range of contextual information within both branches. As a result, the reconstructed images have richer details and more accurate structures.

Evaluation metrics

To evaluate the performance of the proposed method, two image quality metrics are introduced: peak signal-to-noise ratio (PSNR)³¹, structural similarity index metric (SSIM)³². PSNR is a commonly used metric to measure the quality of image reconstruction. It evaluates the similarity between the reconstructed image and the original image at the pixel intensity level. It is defined as follows:

$$MSE = \frac{1}{N} \sum_{i=1}^N [I_{SR}(i) - I_{HR}(i)]^2, \quad (3)$$

$$PSNR = 10 \log_{10} \left(\frac{\max(I_{SR})^2}{MSE} \right), \quad (4)$$

where i and N represent the index of the pixels and the total number of pixels in an image, respectively. I_{SR} represents the image reconstructed by the network, and I_{HR} is the ground truth image.

SSIM focuses on the perceptual structure of the image and assesses the similarity of images in terms of luminance, contrast, and structure. The definition of SSIM is given by:

$$L(I_{SR}, I_{HR}) = \frac{2\mu_{I_{SR}}\mu_{I_{HR}} + C_1}{\mu_{I_{SR}}^2 + \mu_{I_{HR}}^2 + C_1}, \quad (5)$$

$$C(I_{SR}, I_{HR}) = \frac{2\sigma_{I_{SR}}\sigma_{I_{HR}} + C_2}{\sigma_{I_{SR}}^2 + \sigma_{I_{HR}}^2 + C_2}, \quad (6)$$

$$S(I_{SR}, I_{HR}) = \frac{\sigma_{I_{SR}I_{HR}} + C_3}{\sigma_{I_{SR}}\sigma_{I_{HR}} + C_3}, \quad (7)$$

where L , C , and S represent luminance, contrast, and structure, respectively. $\mu_{I_{SR}}$, $\mu_{I_{HR}}$ denote the means of I_{SR} and I_{HR} , respectively. While $\sigma_{I_{SR}}$, $\sigma_{I_{HR}}$ are the variances of I_{SR} and I_{HR} , respectively. $\sigma_{I_{SR}I_{HR}}$ indicates the covariance between I_{SR} and I_{HR} . SSIM is the product of these three components L , C , and S . When C_3 is set to $C_2/2$, the final SSIM is expressed as follows:

$$SSIM = \frac{(2\mu_{I_{SR}}\mu_{I_{HR}} + C_1)(2\sigma_{I_{SR}I_{HR}} + C_2)}{(\mu_{I_{SR}}^2 + \mu_{I_{HR}}^2 + C_1)(\sigma_{I_{SR}}^2 + \sigma_{I_{HR}}^2 + C_2)}. \quad (8)$$

Loss function

To pursue a high PSNR while preserving more accurate retinal structures, our loss function was defined as:

$$L = L_{\alpha} + L_{\beta} + L_{\gamma}, \quad (9)$$

where L_{α} , L_{β} , and L_{γ} represent the losses between the reconstructed coarse image I_{SR}^{Coarse} and I_{HR} , the reconstructed high-frequency image $I_{SR}^{texture}$ and the high-frequency image of the ground truth $I_{HR}^{texture}$, as well as I_{SR} and I_{HR} , respectively. L_{α} , L_{β} , and L_{γ} were the same function as follows:

$$L_{\alpha} = L_{pix} + L_{per} + L_{gra}. \quad (10)$$

Lim et al. found that while minimizing the L2 norm can maximize the PSNR value, using the L1 norm can lead to a better network convergence³³. Consequently, the L1 norm was employed to measure the pixel error between the output and the ground truth. L_{pix} was defined as follows:

$$L_{pix} = \frac{1}{N} \sum_{i=1}^N \|I_{SR}^i - I_{HR}^i\|_1, \quad (11)$$

where I_{SR}^i and I_{HR}^i represent the i -th SR image and the i -th HR image in a batch, respectively.

However, only using L_{pix} may not achieve a good perceptual performance. Hence, a perceptual loss³⁴ was included to enhance the visual similarity of the output images to HR images. Specifically, it utilized a pre-trained

VGG19 network³⁵ to extract high-level information from the L-th layer, and employed the L2 norm to measure the error of the extracted features. L_{per} was defined as follows:

$$L_{per} = \frac{1}{N} \sum_{i=1}^N \left\| \Phi^L(I_{SR}^i) - \Phi^L(I_{HR}^i) \right\|_2^2, \quad (12)$$

where $\Phi^L(I_{SR}^i)$ and $\Phi^L(I_{HR}^i)$ represent the features of the i-th SR image extracted by the L-th layer and the features of the i-th HR image extracted by the L-th layer in a batch, respectively.

To avoid the smoothing effect caused by minimizing L_{pix} , the gradient loss was used to penalize the gradient of images. L_{gra} was defined as follows:

$$L_{gra} = \frac{1}{N} \sum_{i=1}^N \left\| \nabla I_{SR}^i - \nabla I_{HR}^i \right\|_1, \quad (13)$$

where ∇I_{SR}^i and ∇I_{HR}^i represent the gradient operator of the i-th SR image and the gradient operator of the i-th HR image in a batch, respectively. We used the Sobel gradient operator (first-order derivatives) because it could enhance regions of rapid intensity change (edges) while being less affected by minor intensity variations (noise), in contrast to the Laplacian operator (second-order derivatives). ∇I_{SR}^i was defined as follows, where $*$ denotes the convolution operation:

$$G_x = \begin{bmatrix} -1 & 0 & 1 \\ -2 & 0 & 2 \\ -1 & 0 & 1 \end{bmatrix}, G_y = \begin{bmatrix} -1 & -2 & -1 \\ 0 & 0 & 0 \\ 1 & 2 & 1 \end{bmatrix}, \quad (14)$$

$$\nabla I_{SR}^i = \frac{\partial I_{SR}^i}{\partial x} + \frac{\partial I_{SR}^i}{\partial y}, \quad (15)$$

$$\frac{\partial I_{SR}^i}{\partial x} = G_x * I_{SR}^i, \frac{\partial I_{SR}^i}{\partial y} = G_y * I_{SR}^i. \quad (16)$$

Implementation details

During training, the hyperparameters G and M for HASPN were set to 20 and 5, respectively. All the networks were optimized using the Adam optimizer with $\beta_1 = 0.9$ and $\beta_2 = 0.999$, with an initial learning rate of $1e-4$. The learning rate for each layer across all networks decayed by 50% every 20 epochs. The batch size for each network were 2. All models were trained for 200 epochs to ensure their convergences.

The entire process was implemented within the PyTorch 2.1.0 framework, compatible with Python version 3.10, on a Tesla A100 GPU with 40GB of memory.

Results and discussion

To demonstrate the superiority of our proposed network HASPN, it was qualitatively compared with several prevailing methods, including Bicubic, SRCNN³⁶, FSRCNN³⁷, EDSR³³, RDN³⁸, RCAN³⁹, SRGAN⁴⁰, ESRGAN⁴¹, RFANet²⁸, RVSRNet⁴², TDPN³⁰, SwinIR⁴³, ESRT⁴⁴.

As shown in Fig. 4 (pair_72), the outer segment (OS) of the Bicubic reconstructed image exhibited discontinuity. Due to the inherent characteristics of interpolation methods, many ringing artifacts existed at the edges of the external limiting membrane (ELM) and the retinal pigment epithelium (RPE). The ELM in the FSRCNN reconstructed image was excessively blurred and affected by artifacts when deconvolution was used as the upsampling method⁴⁵. These artifacts significantly affected the final quality of the images. Surprisingly, compared to the results of Bicubic and FSRCNN, the ELM reconstructed by SRCNN displayed higher contrast and sharpness. However, the RPE layers in these reconstructed images were severely distorted compared to the HR image. EDSR, RDN, and RCAN employed a wide-channel residual block, dense residual connections, and channel attention in their network designs, respectively, to enhance the network's ability to learn features. This led to better visual performance than Bicubic, SRCNN, and FSRCNN. Additionally, EDSR, RDN, and RCAN achieved results comparable to those of GAN-based methods (SRGAN, ESRGAN) and RFANet. Furthermore, TDPN reconstructed clearer retinal structures than aforementioned methods except for our model. Conversely, it is worth noting that TDPN and RVSRNet failed to reconstruct the tiny granular structures observed in the RPE layer. While SwinIR and ESRT effectively reconstructed fine-grained structures in the RPE layer, they failed to reconstruct the ELM with high contrast and introduced artifacts in the OS. In comparison, our model HASPN could reconstruct these subtle structures better, and the restored ELM exhibited higher contrast than that of other methods. Moreover, the OS reconstructed by HASPN was more continuous.

For pair_67, the internal limiting membrane (ILM) reconstructed by Bicubic, SRGAN, and RFANet exhibited a ladder-like structure. For the reconstruction of the central fovea (denoted by the green arrow), most methods, except for FSRCNN, SwinIR, ESRT and HASPN, showed large differences with the HR image. RDN and ESRGAN failed to accurately reconstruct the inner nuclear layer (INL). Although the differences between TDPN and the HR image in the reconstruction of the INL were smaller, the reconstructed ILM and the central fovea remained slightly blurred. SwinIR and ESRT also did not perform well in reconstructing the INL, resulting in blurred edges in the reconstructed images. In contrast, our model HASPN shown excellent performance in

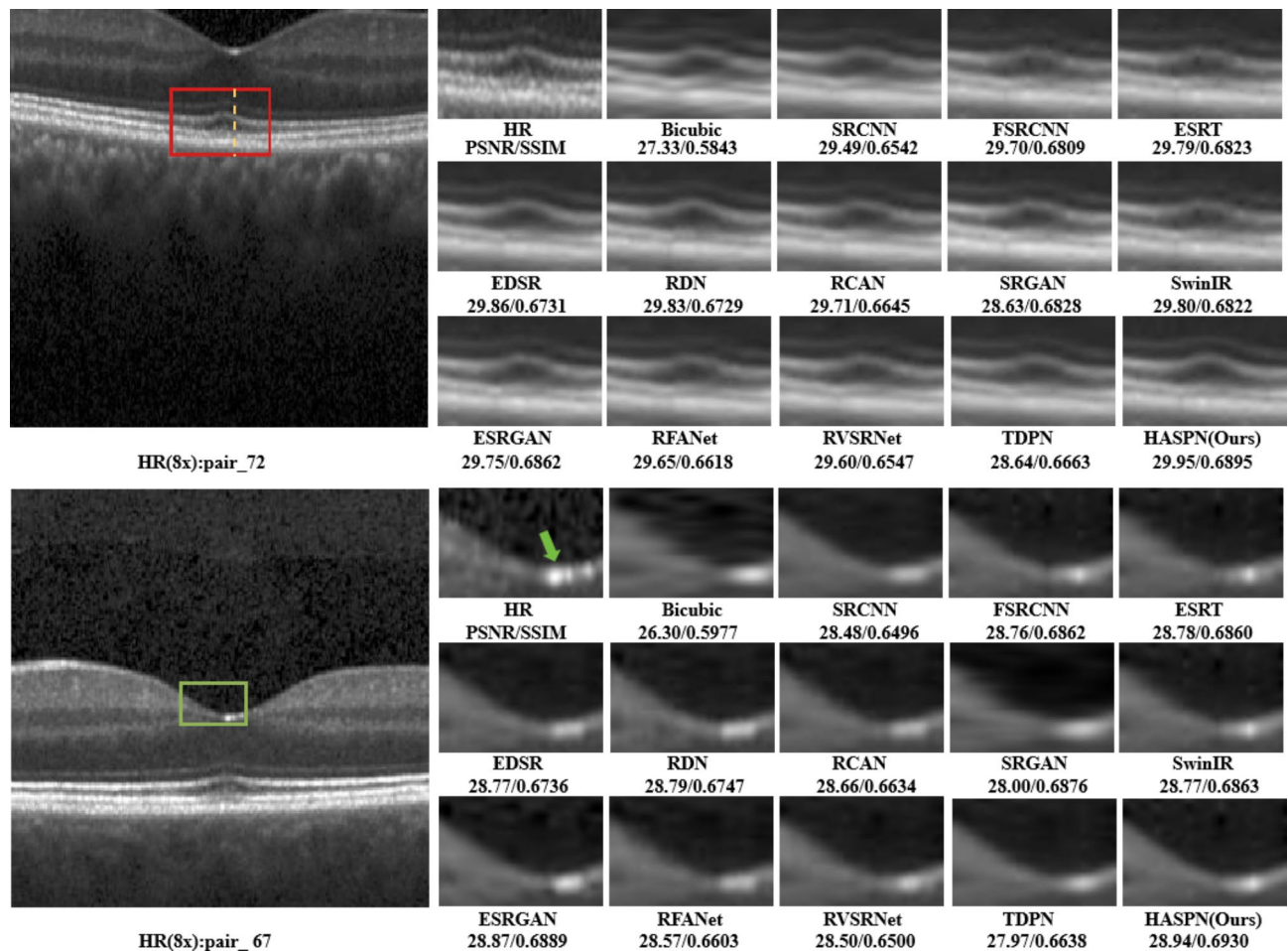


Fig. 4. Visual comparisons of HASPN with prevailing models at 8x SR.

restoring these structures. It not only completely reconstructed the INL but also had the best visual similarity to the HR image in the ILM. These results demonstrate the superiority of HASPN in reconstructing fine structures in retinal images.

Next, to further reflect the performance of our method, we compared HASPN with TDPN, SRGAN (ranked second in terms of PSNR), and ESRT (ranked second in terms of SSIM) by plotting the profile of the selected A-line (indicated by the dashed orange line in HR(8x): pair_72 of Fig. 4). The comparisons were shown in Fig. 5. The peak observed in Fig. 5, specifically in rows 65 to 70, corresponds to the inner/outer segment junction (IS/OS junction) depicted in Fig. 4. It was evident that the structures reconstructed by HASPN and TDPN closely aligned with the ground truth, whereas a notable discrepancy existed between the reconstructions produced by ESRT and the ground truth. Notably, the outer segment (OS), represented by rows 70 to 75, reconstructed by HASPN nearly coincided with the ground truth, in contrast to the slight gaps observed in the OS reconstructions generated by TDPN and ESRT. This underscores the superiority of HASPN in preserving the integrity of retinal layers at the pixel level. Additionally, within the retinal pigment epithelium (RPE) layer, represented by rows 80 to 85, the reconstruction results of TDPN, ESRT, and HASPN closely approximate the ground truth. However, the results obtained from SRGAN exhibited a significant deviation from the ground truth, which may be attributed to the method's tendency to produce excessively smooth edges during the reconstruction process.

In Table 1, we quantitatively compared HASPN with other prevailing methods using model complexity metrics (FLOPs, Param, Average Latency) and image quality metrics (PSNR, SSIM). The results indicated that ESRGAN and RFANet attained the highest and second-highest performance at 2x SR, respectively. Although HASPN did not achieve the highest PSNR at 2x SR, its SSIM was only slightly lower than that of ESRGAN. Notably, FSRCNN demonstrated performance that was second only to HASPN while maintaining the smallest model complexity. However, its visual quality was inferior to several other prevailing methods. Moreover, SRGAN and ESRT attained the second highest PSNR and the second highest SSIM at 8x SR, respectively. Our proposed HASPN yielded the best results compared to other methods at both 4x and 8x SR. However, its substantial FLOPs and relatively high latency may limit its applicability in clinical settings. In the future, we will explore techniques to decrease its computational burden.

To validate the role of two branches in enhancing low-frequency and high-frequency features respectively, we visualized the spectral amplitude difference map between the final SR image and the original branch

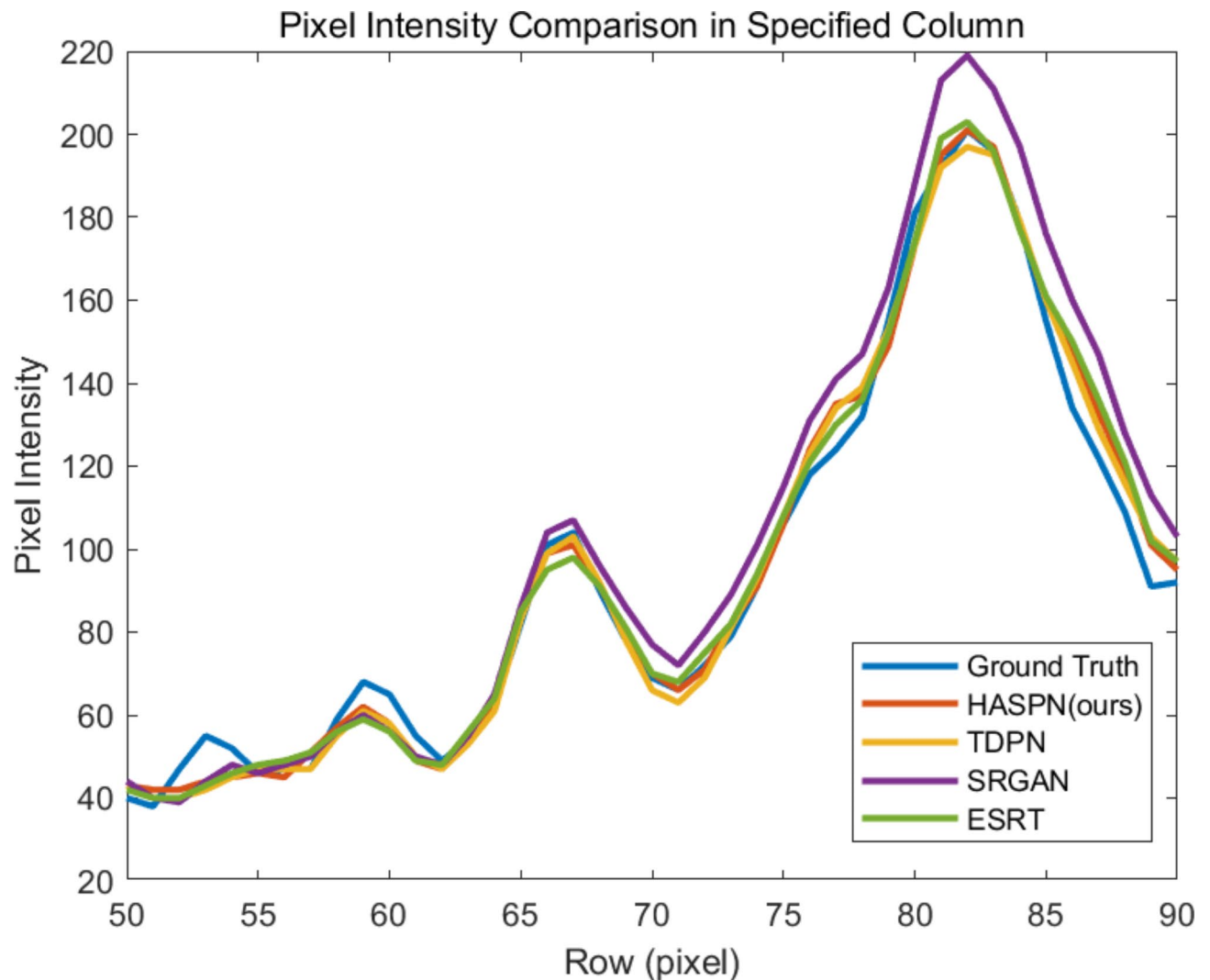


Fig. 5. Profile of the orange dashed line in HR(8x): pair_72 of Fig. 4.

reconstructed image, as well as that between the final SR image and the textures & details branch reconstructed image. As shown in Fig. 6, the final SR image contains more high-frequency components than the original branch reconstructed image, while it contains more low-frequency components than the textures & details branch reconstructed image. This demonstrates that the textures & details branch compensates for the shortcoming of the original branch in extracting high-frequency features, thereby enhancing the overall network performance.

Subsequently, we systematically reduced the quantities of HARB (G), SARb (M), and channel (C) to investigate the impact of different network depths and widths on performance. As presented in Table 2, an increase in the numbers of G, M, and C corresponded with an enhancement in model performance. This finding demonstrates that expanding the depth and width of the network can significantly improve its capabilities in feature extraction and representation. Notably, the model attained its peak PSNR and SSIM values at 4x SR when G, M, and C were set to 20, 5, and 64, respectively. Furthermore, it was observed that G contributed substantially to improvements in both PSNR and SSIM at lower values (8 and 16). Conversely, at smaller values of M (2 and 4), the enhancement in SSIM was relatively limited, and when C was modest (16 and 32), the increase in PSNR was marginal.

To demonstrate the effectiveness of the proposed key components, we performed ablations on ESA, ADCCA, and the textures & details branch, respectively. As shown in Table 3, the PSNR and SSIM values of the images super-resolved by Model 1 were not particularly remarkable. However, with the integration of both ADCCA and ESA, the performance of our model significantly improved. When all key components were integrated, our model displayed the best performance. Furthermore, we ablated our hybrid loss function to validate the effectiveness of its different components. As shown in Table 4, the model achieved the best performance when pixel, perceptual, and gradient losses were used, proving the role of hybrid loss in enhancing the performance of the model.

Last, we tested the generalization capability of our proposed model trained with the normal retinal dataset using DME, CNV, and DRUSEN sub-datasets as mentioned in the “Data preparation” section. As illustrated in

Model	upscale	FLOPs[G]↓	Param[M]↓	Average Latency[S]↓	PSNR↑	SSIM↑
Bicubic	2x	-	-	0.052014	31.73	0.8410
SRCNN	2x	15.0158	0.057281	0.000371	33.62	0.8877
FSCRNN	2x	0.662979	0.010289	0.000487	33.66	0.8884
EDSR	2x	2591.4	39.5402	0.087134	33.59	0.8871
RDN	2x	1444.9	22.0472	0.089945	33.67	0.8897
RCAN	2x	999.595	15.3685	0.060812	32.55	0.8667
SRGAN	2x	32.5143	0.491911	0.002044	32.42	0.8620
ERSGAN	2x	1098	16.6385	0.066602	33.73	0.8913
RFANet	2x	642.309	6.4015	0.061185	33.69	0.8898
RVSRNet	2x	422.278	6.4421	0.022905	32.18	0.8486
TDPN	2x	1900	0.564972	0.096445	31.36	0.8761
SwinIR	2x	48.0272	0.762889	0.040426	33.54	0.8861
ESRT	2x	43.1854	0.639061	0.061485	33.49	0.8862
HASPN	2x	1940.5	0.579052	0.108374	32.65	0.8881
Bicubic	4x	-	-	0.042997	27.68	0.6633
SRCNN	4x	7.5079	0.057281	0.000172	29.44	0.7102
FSCRNN	4x	0.397546	0.012305	0.000474	30.11	0.7637
EDSR	4x	1373.2	40.7204	0.044873	29.95	0.7593
RDN	4x	727.313	22.1211	0.042283	29.92	0.7589
RCAN	4x	504.671	15.4423	0.052618	30.01	0.7507
SRGAN	4x	21.433	0.565767	0.001517	29.68	0.7402
ERSGAN	4x	565.921	16.6551	0.036978	29.74	0.7557
RFANet	4x	325.959	6.4753	0.063954	29.97	0.7604
RVSRNet	4x	211.139	6.4421	0.010950	29.11	0.6939
TDPN	4x	1037.6	0.564972	0.058766	30.06	0.7629
SwinIR	4x	28.8874	0.836745	0.088075	29.96	0.7607
ESRT	4x	24.0506	0.676053	0.036188	29.95	0.7611
HASPN	4x	1060.1	0.579052	0.107809	30.14	0.7650
Bicubic	8x	-	-	0.041999	25.74	0.5686
SRCNN	8x	3.7539	0.057281	0.000168	27.79	0.6276
FSCRNN	8x	0.264832	0.016337	0.000450	28.25	0.6733
EDSR	8x	764.072	41.9005	0.026542	28.29	0.6538
RDN	8x	368.531	22.1949	0.021923	28.27	0.6541
RCAN	8x	257.21	15.5162	0.059235	28.14	0.6421
SRGAN	8x	15.8923	0.639623	0.001417	28.35	0.6624
ERSGAN	8x	452.247	16.6884	0.052569	28.34	0.6645
RFANet	8x	167.715	6.5492	0.062491	28.04	0.6392
RVSRNet	8x	105.57	6.4421	0.005082	27.94	0.6232
TDPN	8x	693.935	0.564972	0.070226	27.64	0.6482
SwinIR	8x	19.3175	0.910601	0.049893	28.30	0.6739
ESRT	8x	14.4833	0.713045	0.018722	28.28	0.6742
HASPN	8x	709.793	0.579052	0.105395	28.55	0.6786

Table 1. Quantitative comparisons of 2x, 4x, and 8x SR. The upward arrow (↑) and the downward arrow (↓) indicate that higher and lower values yield better performance, respectively. The best and second best results were highlighted in bold and italics, respectively.

Fig. 7, HASPN can effectively reconstruct retinal layer structures at 2x, 4x, and 8x SR. When the upscaling factor was 2x, the reconstructed image closely resembled the HR image. However, when performing super-resolution at 8x, certain structures were not adequately reconstructed (indicated by the dashed orange rectangle). Aside from these intricate details, our method can reconstruct most of the retinal layer structures. Consequently, it can be inferred that HASPN possesses an excellent generalization ability, indicating its potential for clinical applications.

Conclusions

In this work, we proposed a novel hybrid attention structure preserving network (HASPN) to speed up the acquisition while obtaining high digital resolution images comparable to those by dense acquisition. HASPN displays a superior lateral super-resolution reconstruction performance compared to many mainstream super-

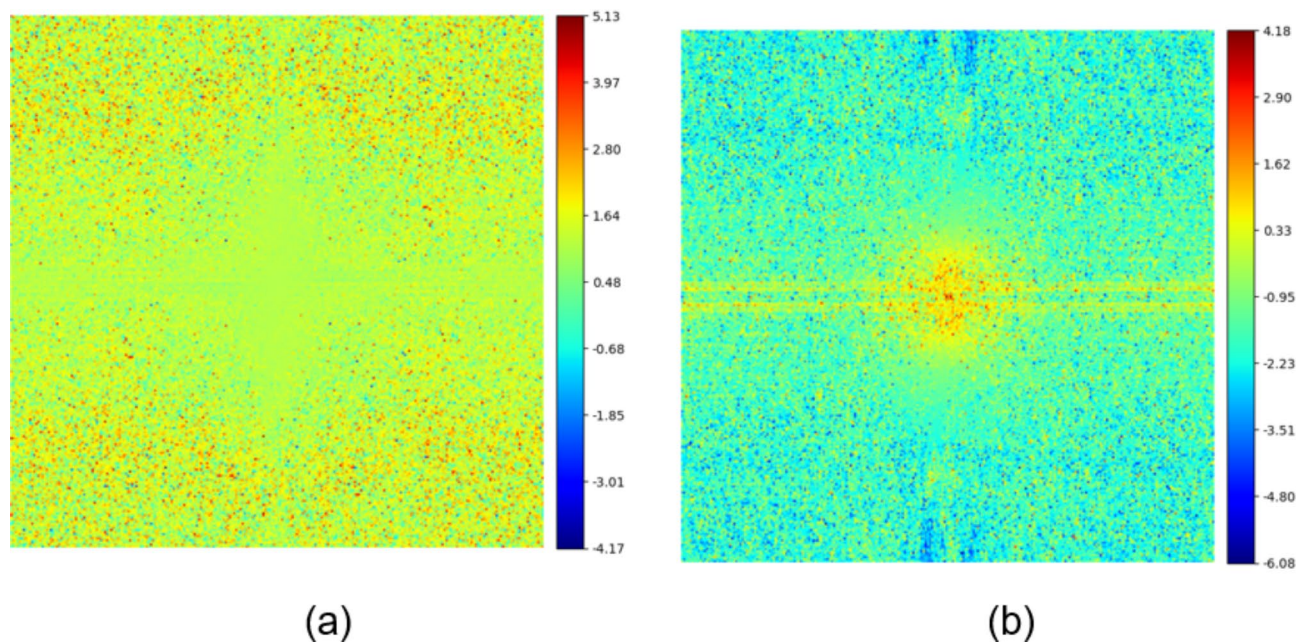


Fig. 6. Spectral amplitude difference maps. **(a)** Difference map between the final SR image and the original branch reconstructed image. **(b)** Difference map between the final SR image and the textures & details branch reconstructed image.

G	M	C	PSNR↑	SSIM↑
20	5	64	30.14	0.7650
16	5	64	29.57	0.7564
8	5	64	28.66	0.7474
20	4	64	29.83	0.7546
20	2	64	29.17	0.7536
20	5	32	29.12	0.7352
20	5	16	29.08	0.7287

Table 2. Quantitative comparisons of HASPN architectures with different widths and depths at 4x SR. G, M, C represent the number of HARB, SARB, and channel in each layer, respectively.

Model	ESA	ADCCA	Tex branch	PSNR↑	SSIM↑
1	×	×	×	28.01	0.6359
2	√	×	×	28.11	0.6404
3	×	√	×	28.23	0.6492
4	√	√	×	28.26	0.6540
5	√	√	√	28.55	0.6786

Table 3. Comparisons of ablating different key components on 8x SR.

resolution methods on the public OCT retinal dataset OCT2017. Through qualitative and quantitative analyses, we demonstrated that HASPN achieved the best results at 4x and 8x SR while effectively preserving the structural information of OCT under-sampled images and restoring more details. Furthermore, we not only investigated the impact of depths and widths on the performance of the network but also conducted ablation studies to demonstrate the effectiveness of our key components and hybrid loss. Finally, we validated that HASPN had an excellent generalization capability and could be applied to reconstruct cross-domain OCT images. Our future research will explore self-supervised methods for reconstructing under-sampled OCT images. Additionally, we will consider applying HASPN to other medical imaging modalities, such as magnetic resonance imaging and computed tomography, to expand its use in medical research and applications.

Loss	Pix	Per	Gra	PSNR↑	SSIM↑
1	✓	×	×	28.18	0.6645
2	×	✓	×	25.68	0.4913
3	×	×	✓	28.17	0.6756
4	✓	✓	✓	28.55	0.6786

Table 4. Comparisons of ablating different components of the loss function on 8x SR.

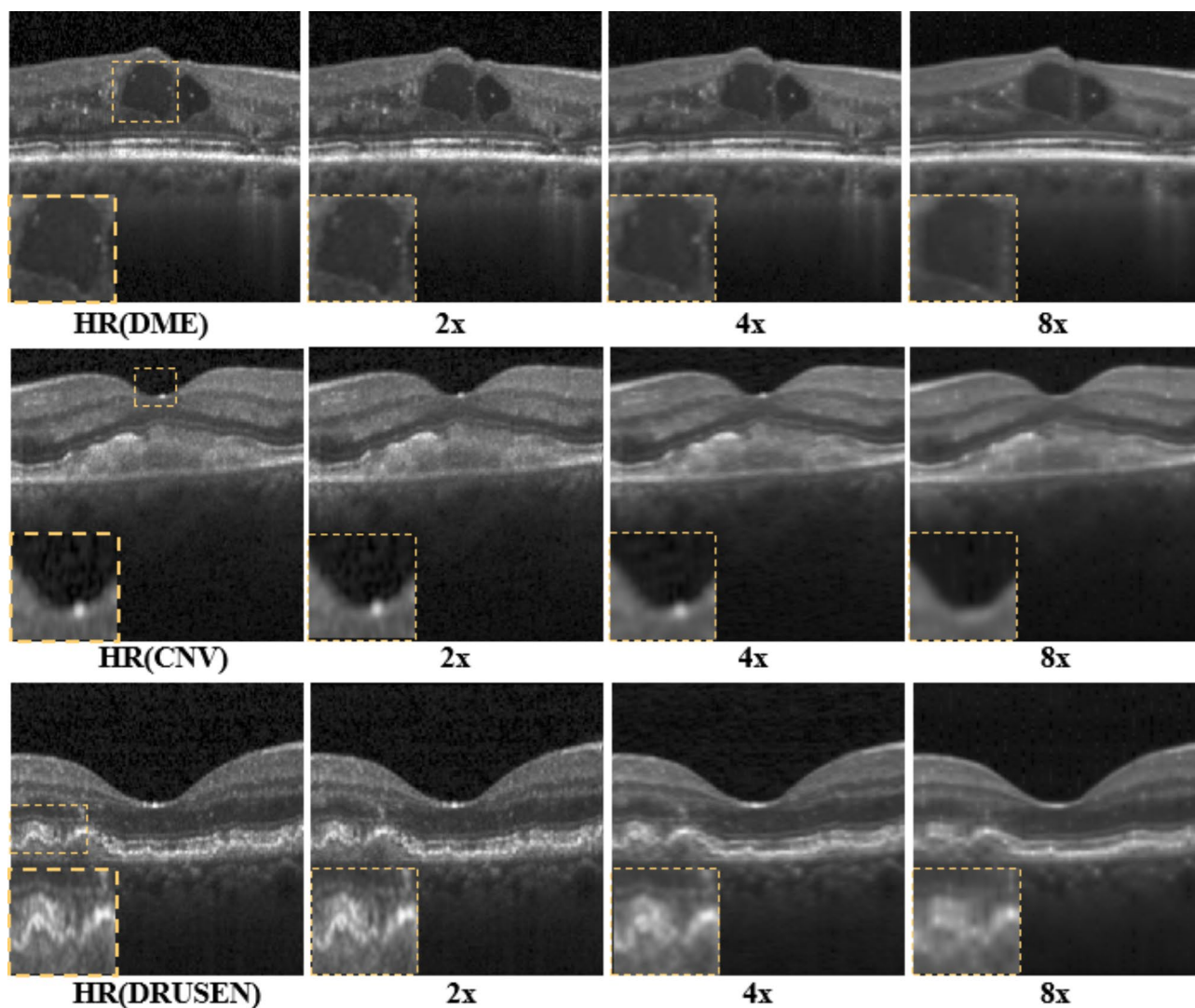


Fig. 7. Generalization performance of the proposed network on diabetic macular edema (DME), choroidal neovascularization (CNV), and multiple drusen in early AMD.

Data availability

The code of this work will be available at <https://github.com/ZacharyG666/HASPN-for-OCT>.

Received: 13 June 2024; Accepted: 9 December 2024

Published online: 03 March 2025

References

- Huang, D. et al. Optical coherence tomography. *Science* **254**(5035), 1178–1181 (1991).
- van Velthoven, M. E., Faber, D. J., Verbraak, F. D., van Leeuwen, T. G. & de Smet, M. D. Recent developments in optical coherence tomography for imaging the retina. *Prog. Retin. Eye Res.* **26**(1), 57–77 (2007).
- Shin, E.-S. et al. OCT-defined morphological characteristics of coronary artery spasm sites in vasospastic angina. *J ACC: Cardiovasc. Imaging* **8**(9), 1059–1067 (2015).

4. Baran, U., Choi, W. J. & Wang, R. K. Potential use of OCT-based microangiography in clinical dermatology. *Skin Res. Technol.* **22**(2), 238–246 (2016).
5. Regatieri, C. V., Branchini, L. & Duker, J. S. The role of spectral-domain OCT in the diagnosis and management of neovascular age-related macular degeneration. *Ophthalmic Surg. Lasers Imaging Retina* **42**(4), S56–S66 (2011).
6. Ghazal, M., Al Khalil, Y., Alhalabi, M., Fraiwan, L., & El-Baz, A. Early detection of diabetics using retinal OCT images. In *Diabetes and Retinopathy*, 173–204 (Elsevier, 2020).
7. Bussell, I. I., Wollstein, G. & Schuman, J. S. OCT for glaucoma diagnosis, screening and detection of glaucoma progression. *Br. J. Ophthalmol.* **98**(Suppl 2), ii15–ii19 (2014).
8. Xu, J., Ishikawa, H., Wollstein, G. & Schuman, J. S. 3D OCT eye movement correction based on particle filtering. 53–56.
9. Fang, L. et al. Fast acquisition and reconstruction of optical coherence tomography images via sparse representation. *IEEE Trans. Med. Imaging* **32**(11), 2034–2049 (2013).
10. Abbasi, A., Monadjemi, A., Fang, L. & Rabbani, H. Optical coherence tomography retinal image reconstruction via nonlocal weighted sparse representation. *J. Biomed. Opt.* **23**(3), 036011–036011 (2018).
11. Wang, L., Chen, Z., Zhu, Z., Yu, X. & Mo, J. Compressive-sensing swept-source optical coherence tomography angiography with reduced noise. *J. Biophotonics* **15**(8), e202200087 (2022).
12. Mei, S., Fan, F., Thies, M., Gu, M., Wagner, F., Aust, O., Erceg, I., Mirzaei, Z., Neag, G. & Sun, Y. Reference-free multi-modality volume registration of X-ray microscopy and light-sheet fluorescence microscopy. arXiv preprint [arXiv:2404.14807](https://arxiv.org/abs/2404.14807) (2024).
13. Wang, L., Sahel, J. A. & Pi, S. Sub2Full: Split spectrum to boost optical coherence tomography despeckling without clean data. *Optics Lett.* **49**(11), 3062–3065 (2024).
14. Hyun, C. M., Kim, H. P., Lee, S. M., Lee, S. & Seo, J. K. Deep learning for undersampled MRI reconstruction. *Phys. Med. Biol.* **63**(13), 135007 (2018).
15. Huang, Y. et al. Simultaneous denoising and super-resolution of optical coherence tomography images based on generative adversarial network. *Optics Express* **27**(9), 12289–12307 (2019).
16. Qiu, B. et al. N2NSR-OCT: Simultaneous denoising and super-resolution in optical coherence tomography images using semisupervised deep learning. *J. Biophotonics* **14**(1), e202000282 (2021).
17. Xu, K., Qin, M., Sun, F., Wang, Y., Chen, Y.-K. & Ren, F. Learning in the frequency domain. 1740–1749.
18. Dosovitskiy, A., Beyer, L., Kolesnikov, A., Weissenborn, D., Zhai, X., Unterthiner, T., Dehghani, M., Minderer, M., Heigold, G. & Gelly, S. An image is worth 16x16 words: Transformers for image recognition at scale. arXiv preprint [arXiv:2010.11929](https://arxiv.org/abs/2010.11929) (2020).
19. Wang, L., Wang, B., Chhablani, J., Sahel, J. A., Pi, S. Freqformer: Frequency-Domain Transformer for 3-D Visualization and Quantification of Human Retinal Circulation. *Electrical Engineering and Systems Science* (2024).
20. Yao, B. et al. PSCAT: A lightweight transformer for simultaneous denoising and super-resolution of OCT images. *Biomed. Optics Express* **15**(5), 2958–2976 (2024).
21. Liu, Z., Lin, Y., Cao, Y., Hu, H., Wei, Y., Zhang, Z., Lin, S. & Guo, B. Swin transformer: Hierarchical vision transformer using shifted windows, 10012–10022.
22. Woo, S., Park, J., Lee, J.-Y. & Kweon, I. S. Cbam: Convolutional block attention module, 3–19.
23. Lu, Y. et al. Super-resolution reconstruction of OCT images based on pyramid long-range transformer. *Chin. J. Lasers* **50**(15), 1507107 (2023).
24. Huang, W. et al. Deep local-to-global feature learning for medical image super-resolution. *Comput. Med. Imaging Graph.* **115**, 102374 (2024).
25. Retinal OCT Images (optical coherence tomography). Kaggle, Vol. <https://www.kaggle.com/paultimothymooney/kermany2018> (2017).
26. Ramponi, G., Strobel, N. K., Mitra, S. K. & Yu, T.-H. Nonlinear unsharp masking methods for image contrast enhancement. *J. Electron. Imaging* **5**(3), 353–366 (1996).
27. Zhu, H., Xie, C., Fei, Y. & Tao, H. Attention mechanisms in CNN-based single image super-resolution: A brief review and a new perspective. *Electronics* **10**(10), 1187 (2021).
28. Liu, J., Zhang, W., Tang, Y., Tang, J. & Wu, G. Residual feature aggregation network for image super-resolution, 2359–2368.
29. Hu, J., Shen, L. & Sun, G. Squeeze-and-excitation networks, 7132–7141.
30. Cai, Q. et al. TDPN: Texture and detail-preserving network for single image super-resolution. *IEEE Trans. Image Process.* **31**, 2375–2389 (2022).
31. Wang, Z., Chen, J. & Hoi, S. C. Deep learning for image super-resolution: A survey. *IEEE Trans. Pattern Anal. Mach. Intell.* **43**(10), 3365–3387 (2020).
32. Wang, Z., Bovik, A. C., Sheikh, H. R. & Simoncelli, E. P. Image quality assessment: from error visibility to structural similarity. *IEEE Trans. Image Process.* **13**(4), 600–612 (2004).
33. Lim, B., Son, S., Kim, H., Nah, S. & Mu Lee, K. Enhanced deep residual networks for single image super-resolution, 136–144.
34. Johnson, J., Alahi, A. & Fei-Fei L. Perceptual losses for real-time style transfer and super-resolution, 694–711.
35. Simonyan, K. & Zisserman, A. Very deep convolutional networks for large-scale image recognition. arXiv preprint [arXiv:1409.1556](https://arxiv.org/abs/1409.1556) (2014).
36. Dong, C., Loy, C. C., He, K. & Tang, X. Image super-resolution using deep convolutional networks. *IEEE Trans. Pattern Anal. Mach. Intell.* **38**(2), 295–307 (2015).
37. Dong, C., Loy, C. C. & Tang, X. Accelerating the super-resolution convolutional neural network, 391–407.
38. Zhang, Y., Tian, Y., Kong, Y., Zhong, B. & Fu, Y. Residual dense network for image super-resolution, 2472–2481.
39. Zhang, Y., Li, K., Li, K., Wang, L., Zhong, B. & Fu, Y. Image super-resolution using very deep residual channel attention networks, 286–301.
40. Ledig, C., Theis, L., Huszar, F., Caballero, J., Cunningham, A., Acosta, A., Aitken, A., Tejani, A., Totz, J. & Wang, Z. Photo-realistic single image super-resolution using a generative adversarial network, 4681–4690.
41. Wang, X., Yu, K., Wu, S., Gu, J., Liu, Y., Dong, C., Qiao, Y. & Change Loy, C. Esrgan: Enhanced super-resolution generative adversarial networks.
42. Wang, L. et al. Axial super-resolution optical coherence tomography via complex-valued network. *Phys. Med. Biol.* **68**(23), 235016 (2023).
43. Liang, J., Cao, J., Sun, G., Zhang, K., Van Gool, L. & Timofte, R. Swinir: Image restoration using swin transformer, 1833–1844.
44. Lu, Z., Li, J., Liu, H., Huang, C., Zhang, L. & Zeng, T. Transformer for single image super-resolution, 457–466.
45. Odena, A., Dumoulin, V. & Olah, C. Deconvolution and checkerboard artifacts. *Distill* **1**(10), e3 (2016).

Acknowledgements

This work was supported by Hebei Provincial Social Science Foundation Project (No. HB20TQ003).

Author contributions

Zezhao Guo designed the methods, conducted the experiments and wrote the manuscript. Zhanfang Zhao reviewed the manuscript.

Declarations

Competing interests

The authors declare no competing interests.

Additional information

Correspondence and requests for materials should be addressed to Z.Z.

Reprints and permissions information is available at www.nature.com/reprints.

Publisher's note Springer Nature remains neutral with regard to jurisdictional claims in published maps and institutional affiliations.

Open Access This article is licensed under a Creative Commons Attribution-NonCommercial-NoDerivatives 4.0 International License, which permits any non-commercial use, sharing, distribution and reproduction in any medium or format, as long as you give appropriate credit to the original author(s) and the source, provide a link to the Creative Commons licence, and indicate if you modified the licensed material. You do not have permission under this licence to share adapted material derived from this article or parts of it. The images or other third party material in this article are included in the article's Creative Commons licence, unless indicated otherwise in a credit line to the material. If material is not included in the article's Creative Commons licence and your intended use is not permitted by statutory regulation or exceeds the permitted use, you will need to obtain permission directly from the copyright holder. To view a copy of this licence, visit <http://creativecommons.org/licenses/by-nc-nd/4.0/>.

© The Author(s) 2025